A Generalized Motion Control Framework of Dielectric Elastomer Actuators: Dynamic Modeling, Sliding-Mode Control and Experimental Evaluation

Jiang Zou, *Member, IEEE*, Shakiru Olajide Kassim, Jieji Ren, Vahid Vaziri, Sumeet S. Aphale, *Senior Member, IEEE*, and Guoying Gu, *Senior Member, IEEE*

***Abstract*—The continuous electromechanical deformation of dielectric elastomer actuators (DEAs) suffers from rate-dependent viscoelasticity, mechanical vibration, and configuration dependency, making the generalized dynamic modeling and precise control elusive. In this work, we present a generalized motion control framework for DEAs capable of accommodating different configurations, materials and degrees of freedom (DOFs). First, a generalized, control-enabling dynamic model is developed for DEAs by taking both nonlinear electromechanical coupling, mechanical vibration and rate-dependent viscoelasticity into consideration. Further, a state observer is introduced to predict the unobservable viscoelasticity. Then, an enhanced exponential reaching law-based sliding-mode controller (EERLSMC) is proposed to minimize the viscoelasticity of DEAs. Its stability is also proved mathematically. The experimental results obtained for different DEAs (four configurations, two materials, and multi-DOFs) demonstrate that our dynamic model can precisely describe their complex dynamic responses and the EERLSMC can achieve precise tracking control; verifying the generality and versatility of our motion control framework.**

***Index Terms*—Dielectric elastomer actuators (DEAs), generalized dynamic modeling, rate-dependent viscoelasticity, sliding-mode control, soft robots.**

I. Introduction

DIELECTRIC elastomer actuators (DEAs) are a family of artificial muscles that have recently generated great interest within the field of soft robotics, due to their large deformation, high-energy density, and fast response speed [1], [2]. Typically, DEAs mainly consist of a prestretched dielectric elastomer membrane coated on both sides with compliant electrodes and a supporting frame [3]. When a high voltage (typically in kV) is applied, the Maxwell stress between the electrodes squeezes the membrane, leading to expand in area and decrease in thickness. The supporting frame then converts this continuous electromechanical deformation into desired actuation. Based on this working principle, DEAs with different configurations (planar, conical, stacked, minimum energy structure, etc.,), materials (acrylic and silicone elastomer) and degrees of freedom (DOFs) have been proposed to generate different actuation, such as elongation, contraction, bending, twisting, and multiple-DOFs movement; enabling the design of novel soft robots, including climbing robots, flying robots, deep-sea robots and wearable robots [4], [5], [6], [7]. As more applications emerge, the dynamic modeling and precise control of DEAs have become highly desirable to facilitate precise manipulation and smooth locomotion [8].

However, the dynamic responses of DEAs suffer from significant nonlinearities. First, the actuation of DEAs comes from one kind of nonlinear electromechanical coupling that not only depends on the square of the voltage, but also relies on the continuous deformation of their configurations [9]. Moreover, the inherent viscoelasticity leads to both creep and hysteresis that deteriorate the actuating accuracy of DEAs [10]. The creep is a slow-time effect that only dominates the dynamic responses during the first few cycles and then can be ignored [11]. The hysteresis is an asymmetric, multivalued, and rate-dependent nonlinearity that exists during the whole responses. In addition, there are resonance-induced mechanical vibrations that also get coupled with viscoelasticity [12], [13]. Finally, DEAs usually forms complex geometric shapes (such as the saddle surface of the minimum energy structure), called geometric nonlinearity, making it difficult to describe the stress and strain distribution within the dielectric elastomer membrane [14]. As a consequence, the dynamic modeling and precise control of DEAs have attracted a lot attentions in the past two decades [15].

A number of relevant models have been reported in previous works, and can be divided into four categories viz:

Manuscript received 29 August 2023; revised 18 November 2023; accepted 21 November 2023. Date of publication 4 December 2023; date of current version 3 January 2024. This paper was recommended for publication by Associate Editor Y. Liu and Editor A. Menciassi upon evaluation of the reviewers' comments. This work was supported in part by the National Natural Science Foundation of China under Grant 52275024 and Grant 52025057, in part by the Natural Science Foundation of Shanghai under Grant 23ZR1435500 and Grant 22511101700, and in part by the Nigerian Petroleum Technology Development Fund (PTDF) by the Ph.D. Research under Grant PTDF/ED/OSS/PHD/SOK/052/18). *(Jiang Zou and Shakiru Olajide Kassim contributed equally to this work.) (Corresponding author: Guoying Gu.)*

Jiang Zou, Jieji Ren, and Guoying Gu are with the State Key Laboratory of Mechanical System and Vibration, Shanghai Jiao Tong University, Shanghai 200240, China, and also with the Robotics Institute, School of Mechanical Engineering, Shanghai Jiao Tong University, Shanghai 200240, China (e-mail: zoujiang@sjtu.edu.cn; jiejiren@sjtu.edu.cn; guguoying@sjtu.edu.cn).

Shakiru Olajide Kassim, Vahid Vaziri, and Sumeet S. Aphale are with the Artificial Intelligence, Robotics and Mechatronic Systems (ARMS) Group, School of Engineering, University of Aberdeen, AB24 3UE Aberdeen, U.K. (e-mail: r03sk21@abdn.ac.uk; vahid.vaziri@abdn.ac.uk; s.aphale@abdn.ac.uk).

Digital Object Identifier 10.1109/TRO.2023.3338973

hyperelastic models, viscoelastic models, phenomenological models, and lumped-parameter models. Hyperelastic models, one kind of early models, adopt a hyperelastic material assumption to describe the strain/stress distribution within the dielectric elastomer membrane, which have been widely used to explain the electromechanical deformation and instability of DEAs. However, hyperelastic models can only describe the static responses of DEAs because the viscoelasticity is not taking into consideration [16], [17]. To address this deficiency, the viscoelasticity is treated as a type of energy dissipative phenomenon that can be described by introducing a series of rheological units into the constitutive relationship. Based on the viscoelastic constitutive relationship of dielectric elastomer membrane, many viscoelastic models have been proposed to precisely describe the complex dynamic responses, such as creep and rate-dependent hysteresis. It should be noted that viscoelastic constitutive relationship usually consists of several ordinary or partial differential equations that lead to computational challenges when the geometric nonlinearity is taken into account. As a result, analytical models can only be established for a limited variety of DEAs with simple strain/stress distribution [10], [18]. In addition, viscoelastic models usually are too complicated to be converted into control models. Different from these physics-based models, phenomenological models, such as the Prandtl–Ishlinskii and Backlash models, have been introduced to describe the rate-dependent viscoelasticity of DEAs [13], [19], [20]. These phenomenological models have benefit of expandability and reduced number of parameters as they only rely on the experimental data (typically input–output relationships) with no consideration of the physical properties of DEAs. However, these models do not include the dynamics associated with the resonance-induced mechanical vibrations. This imposes a significant limitation on their adoption for broader control-oriented applications. To overcome the drawback of these phenomenological models, some lumped-parameter models have been developed by simplifying DEAs into a lumped-parameter mechanical system. In pursuit of this objective, the present study assumes the deformation of DEAs to be a form of simple strain distribution. Subsequently, viscoelastic constitutive models are employed to articulate the stress-strain relationship. For instance, the lumped parameter model for conical DEAs assumes a truncated-cone geometry [21]. In contrast, the model for stacked DEAs relies on a uniform strain distribution and a linear material model [22]. However, the applicability of these models is constrained by the specific configurations of DEAs, limiting their generalizability. Moreover, none of these models exhibits the capability to quantitatively depict coupled vibration and rate-dependent viscoelasticity, thereby impeding their practical utility. Consequently, the development of a comprehensive dynamic framework for DEAs, accommodating diverse configurations, materials, and DOFs, is imperative. Such a framework should have the capacity to characterize intricate dynamic responses across a broad frequency spectrum, encompassing phenomena, such as rate-dependent viscoelasticity, mechanical vibration, and their interplay. Regrettably, such a holistic framework remains elusive in current research.

Based on above dynamic models, different control strategies have been introduced for precise control of DEAs, including model-based inverse controllers, nonlinear controllers, and model-free controllers. Utilizing identified linear models or phenomenological models enables the development of direct inverse controllers to mitigate the nonlinearity of DEAs. However, linear models often overlook the influence of viscoelasticity, restricting the corresponding controllers to tracking static trajectories rather than periodic ones. In contrast, phenomenological model-based inverse controllers can effectively address rate-dependent viscoelasticity. Their precision can be enhanced by integrating proportion–integration–differentiation (PID) controllers. It is important to note that phenomenological model-based inverse controllers, lacking consideration for the mechanical structure, tend to avoid mechanical vibrations. This limitation significantly constrains the operational frequency of DEAs, typically remaining below their natural frequency [20], [23], [24]. While lumped parameter models have paved the way for nonlinear controllers, such as nonlinear PID, adaptive sliding-mode control, and H-infinity control [22], [25], [26], [27], these controllers are generally applicable to static or periodic trajectories with a minimal strain. This restricts their broader application, hindering their effectiveness for dynamic trajectories with higher strain levels. Model-free controllers, such as the proxy-based sliding-mode controller, also have shown the potential to achieve high-precision tracking control of DEAs without complex dynamic models [28]. However, model-free controllers are limited by their poor robustness and adaptability because the dynamic features of DEAs are not taken into consideration. As a consequence, designing control schemes that eliminate the complex nonlinearities exhibited by DEAs, and result in highly precise trajectory tracking, is an open research challenge.

To address the challenges identified earlier, this work proposes a generalized motion control framework for DEAs. First, we establish a generalized, control-enabling dynamic model that can fully characterize the complex dynamic features (including the nonlinear electromechanical response, viscoelasticity, resonance-induced mechanical vibrations, and their coupling) of DEAs. Then, a state observer is introduced to predict unobservable states that depend on the viscoelasticity. Finally, based on the generalized dynamic model and state observer, and considering the versatility of reaching law-based sliding-mode control, we introduced an enhanced exponential reaching law-based sliding-mode controller (EERLSMC) [29] with boundary layer, which provides faster convergence and enhanced chattering-free property to eliminate the detrimental nonlinearities of DEAs and deliver excellent reference trajectory tracking. Planar DEA (made of silicone elastomer), conical DEA (made of acrylic elastomer), DEA with a minimum energy structure (DEA-MES, made of acrylic elastomer), and DEA with two DOFs (2DOF-DEA, made of acrylic elastomer) are employed to validate our generalized dynamic model and control strategy.

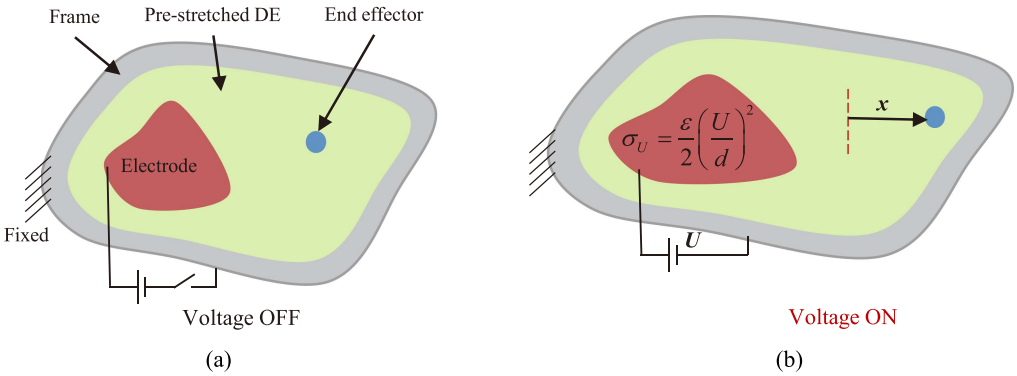

Fig. 1. Working principle of DEAs. (a) Initial state without voltage. (b) Output displacement when an exciting voltage (typically in kV) is applied.

The experimental results for tracking different periodic trajectories demonstrate the generality and versatility of our motion control framework for DEAs.

The main contributions of this work are as follows.

1) To the best of the authors knowledge, this is the first development of a generalized dynamic model that holistically describe the complex dynamic responses (including continuous electromechanical deformation, rate-dependent viscoelasticity, mechanical vibrations, and their coupling) of DEAs with different configurations, materials, DOFs, and wide frequency range.
2) The control-enabling property of our generalized dynamic model paves the way for controller design and stability analysis (such as the EERLSMC), demonstrating superior tracking performance for four DEA configurations against a number of different periodic reference trajectories.

The rest of this article is organized as follows. Section II presents the development of the generalized dynamic model for DEAs. The EERLSMC is developed in Section III. Section IV presents the experimental verification of the generalized dynamic model and EERLSMC. Finally, Section V concludes this article.

II. Generalized Dynamic Modeling of DEAs

In general, DEAs mainly consist of a prestretched dielectric elastomer membrane, a supporting frame, compliant electrodes, and an end effector [see Fig. 1(a)]. When an excitation voltage is applied, the Maxwell stress between the electrodes squeezes the dielectric elastomer membrane and generates a continuous deformation while the supporting frame (usually made of stiff or flexible materials) converts the continuous deformation into desired displacement of the end effector [see Fig. 1(b)]. It must be noted that although the deformation of DEAs is continuous with infinite DOFs, the movement DOFs of the end effector is finite. Without losing generality, we firstly discuss DEAs with a single DOF and then expand the concept to DEAs with multiple DOFs.

To describe the dynamic responses of a DEA with a single DOF, the key is to describe the time-dependent relationship between the excitation voltage U and displacement x of the end effector and the continuous deformation of the dielectric elastomer membrane is unnecessary. Based on this concept, dynamic responses of DEAs can be treated as dynamic responses of end effectors under applied forces. According to the working principle of DEAs, there are three kinds of distribution forces applied to the end effector, including the $\tilde{f}(x)$, $\tilde{f}(x,U)$ and viscoelastic force. $\tilde{f}(x)$ comes from the elastic force of the dielectric elastomer membrane without any voltage applied. $\tilde{f}(x,U)$ represents the actuation force under the excitation voltage, which is coupled with x because of the nonlinear electromechanical response. Viscoelastic force originates from inherent viscoelasticity of DEAs that is treated as one kind of energy dissipative phenomenon and described by several rheological units [9], [10]. To obtain those applied forces, the general approaches mainly involve two steps: 1) a viscoelastic constitutive model (such as Neo-Hookean, Gent, and Ogden) is adopted to describe the stress/strain distribution within the dielectric elastomer membrane; 2) then $\tilde{f}(x)$, $\tilde{f}(x,U)$, viscoelastic force and x can be calculated based on the stress/strain distribution. In general, those approaches are only effective for DEAs without geometric nonlinearity, limiting their generality and versatility. To solve this problem, we mainly focus on capturing the relationship between U and x and simplify the end effector into a mechanical system with finite DOFs.

In general, a dynamic model of a mechanical system with a DOF relating input force F (which in the case of DEA is a function of the excitation voltage U) to output displacement x can be expressed as

$$m\ddot{x} + \eta_0\dot{x} + Kx = F(U) \tag{1}$$

where U and x represent the input (excitation voltage) and output (end-effector's displacement), respectively. m, η_0, K, and $F(U)$ are the mass, damping ratio, stiffness, and actuation force, respectively. The key challenge in adopting (1) to describe the dynamic responses of DEAs are as follows.

1) K is a nonlinear function of x rather than a constant parameter because of the hyperelasticity or viscoelasticity.
2) Due to the continuous electromechanical deformation, $F(U)$ not only depends on the excitation voltage, but also on the end effector's displacement x.

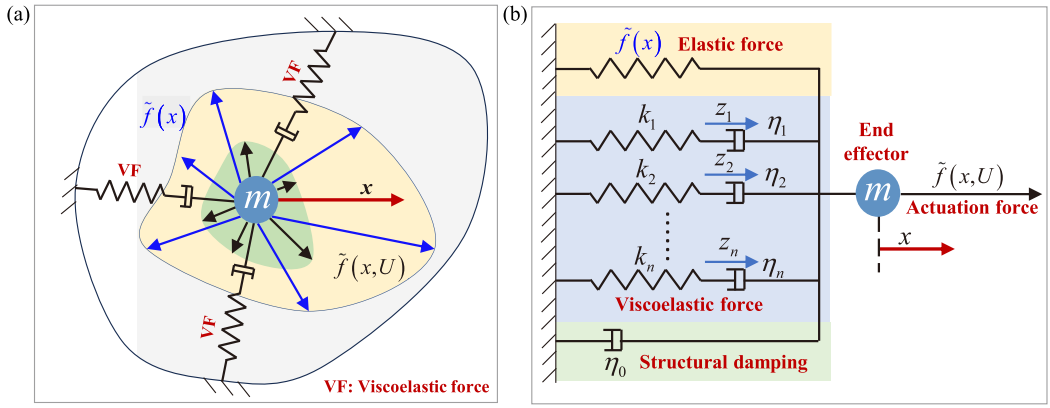

Fig. 2. Development of the dynamic model. (a) Force analysis of the end effector. (b) Equivalent mass-nonlinear spring-damping system.

3) The inherent viscoelasticity is not taken into consideration in this formulation.

To address these shortcomings, our generalized dynamic model makes the following assumptions.

1) For the quasi-static response, $\tilde{f}(x)$ represents the static force-displacement relationship when the excitation voltage equals zero. The widely used method is to establish $\tilde{f}(x)$ based on the institutive material model (such as Neo-Hookean, Gent, and Ogden), but it only works for DEAs without geometric nonlinearity [21]. To ensure the generality, we adopt an experimental method that can obtain $\tilde{f}(x)$ by curve fitting experimental data. Based on previous works and our experiences [18], [30], $\tilde{f}(x)$ can be expressed as

$$\tilde{f}(x) = qx^2 + px \tag{2}$$

where q and p are appropriately selected constants that ensure an accurate fit with the measured experimental data.

2) The actuation force $\tilde{f}(x,U)$ arises from the deformation of the dielectric elastomer membrane under Maxwell stress. The Maxwell stress is usually proportional to U^2 but inversely proportional to the thickness of the dielectric elastomer membrane [3]. Considering the incompressibility of the dielectric elastomer membrane, we formulate $\tilde{f}(x,U)$ as

$$\tilde{f}(x,U) = U^2\left(ax^2 + bx + c\right) \tag{3}$$

where a, b, and c represent three constants.

3) The viscoelasticity is an inherent nonlinearity of the dielectric elastomer membrane, generally described by adding several rheological units into the institutive model [9], [10]. For DEAs, we assume that the influence of viscoelasticity on the dynamic response also can be characterized by introducing proper rheological units (corresponding to viscoelastic forces).

4) DEAs also suffer from structural damping of the supporting frame and frictional force coming from air or contact surface. We introduce a term, $\eta_0\dot{x}$, to represent these damping effects.

Remark: We should mention that the selection of (2) and (3) is not unique. Based on the experimental data, different functions may be available. For the convenience of controller design and stability analysis, we prefer to select simple functions to describe them. The main advantage of this method depends on the fact that it avoids taking complex constitutive model and geometric nonlinearity into consideration, significantly decreasing their complexity and improving their generality. Moreover, (2) and (3) can be substituted with linear functions when the strain is small. However, employing linear functions in these cases could restrict their applicability to situations involving large deformations, thereby diminishing their generality.

Based on above assumptions, we establish an equivalent mechanical system of the end effector [see Fig. 2(b)], consisting of a lumped mass-nonlinear spring-damping system and several rheological units. Therefore, the generalized dynamic model of DEAs can be expressed as

$$m\ddot{x} + \eta_0\dot{x} + px + qx^2 + \sum_{i=1}^{n} k_i z_i = U^2(ax^2 + bx + c)$$
$$k_i z_i = \eta_i(\dot{x} - \dot{z}_i) \tag{4}$$

where k_i and z_i represent the stiffness and displacement of each spring within rheological units. η_i is damping ratio of each damper within rheological units. $i = 1, 2, \ldots, n$ represents the number of rheological units. The generalized dynamic model can be used to describe the complex dynamics of DEAs with different configurations, materials, and DOFs where unknown parameters are identified using experimental data. We should mention that the generalized dynamic model of DEAs as presented in (4) will be validated in the Section IV. Based on the generalized dynamic model, the following section presents the design of a model-based controller capable of minimizing the effects of inherent nonlinearities, thereby enabling accurate trajectory tracking.

III. Controller Design and Stability Analysis

Our generalized dynamic model is one kind of control-enabling models, so it paves way for nonlinear controller design and stability analysis. We should mention that the generalized dynamic model consists of several differential equations. It is

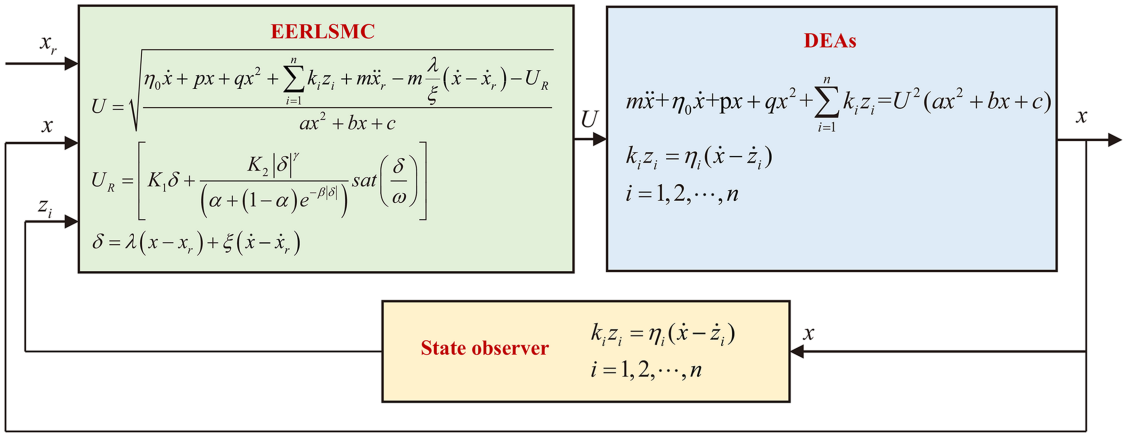

Fig. 3. Block diagram of the employed control scheme clearly showing the DEAs (indicated by the proposed generalized dynamic model), the developed control strategy (EERLSMC) and the implemented state observer that facilitates the control implementation.

not easy to obtain its inverse model for minimizing nonlinearities. Therefore, traditional feedforward plus feedback control strategy is unavailable [13]. Known for their simplicity, low sensitivity to system parameter variations and greater robustness, sliding-mode control (SMC) schemes are widely employed in several nonlinear control applications. Among them, the exponential reaching law-based sliding-mode controller furnishes chattering-free control input and guarantees zero convergence of system states in finite time [29], [31], [32]. Without loss of generality, an EERLSMC is introduced to validate the control-enabling property of our dynamic model and compensate for the complex nonlinearity of DEAs. To this end, we first need to obtain z_i in (4). However, they are not measurable. To solve this problem, the general approach is to predict those z_i through the state observer. We should mention that traditional state observer is constructed based on linear systems, not the nonlinear system shown in (4). To avoid complex linearization procedure, we directly use the measured x to predict the z_i through $k_iz_i = \eta_i(\dot{x} - \dot{z}_i), i = 1, 2, \ldots, n$. Following experimental results also can prove the effectiveness of the state observer. Then, the EERLSMC is developed and its stability is mathematically ascertained in this section.

Remark: The preference for EERLSMC stems from several key considerations viz as follows.

1) Limitations of PID controllers: PID controllers, as highlighted in [13], are constrained to tracking static trajectories and are not well-suited for periodical trajectories.
2) Challenges with traditional SMCs: Traditional SMCs, as discussed in [33], are prone to undesirable high-frequency chattering, leading to a reduction in control accuracy.
3) Comparison with super-twisting SMCs: While super-twisting SMCs, mentioned in [34], can address high-frequency chattering, EERLSMC demonstrates superior convergence and offers ease of stability analysis.

Given these factors, EERLSMC is selected to illustrate the controller design and stability analysis process, thereby validating the effectiveness of the generalized dynamic model in our work. It is important to note that this choice is made without sacrificing generality, as the outlined process can be applied analogously to introduce various other SMCs into the realm of DEAs in the future. This flexibility allows for the exploration and implementation of different SMCs, maintaining the adaptability and relevance of our approach in the evolving landscape of DEA control systems.

A. Controller Design

The goal of the designed controller is to accurately track any reference trajectory x_r while significantly suppressing the nonlinearities of DEAs and ensuring that the tracking error approaches zero at finite time. Based on the generalized dynamic model, the development of the EERLSMC with the state observer is outlined below (see Fig. 3).

At first, the switching hyperplane (sliding surface) is defined as

$$\delta = \xi\dot{\varepsilon}(t) + \lambda\varepsilon(t) \tag{5}$$

where ξ and λ are user-selected constants that meet the Hurwitz stability criteria. The ε and $\dot{\varepsilon}$ represent the tracking error and its derivative, respectively, which can be expressed as

$$\begin{aligned} \varepsilon &= x - x_r \\ \dot{\varepsilon} &= \dot{x} - \dot{x}_r \end{aligned} \tag{6}$$

where x_r and $\dot{x}_r$ are the reference displacement and velocity, respectively. By (5) to zero, the system error dynamics can be expressed as

$$\varepsilon(t) = \varepsilon(0)e^{\left(-\frac{\lambda}{\xi}t\right)}. \tag{7}$$

Thus, ε and $\dot{\varepsilon}$ exponentially converge to zero at a constant rate of $\frac{\lambda}{\xi}$.

The derivative of (5) can be written as

$$\dot{\delta} = \xi\left(\ddot{x} - \ddot{x}_r\right) + \lambda\left(\dot{x} - \dot{x}_r\right). \tag{8}$$

The force input, which is used to deduce the inverting control input, is obtained by putting (4) into (8) and setting $\dot{\delta} = 0$. Solving this results in

$$\hat{F} = \eta_0\dot{x} + px + qx^2 + \sum_{i=1}^{n} k_iz_i + m\left[\ddot{x}_r - \frac{\lambda}{\xi}\left(\dot{x} - \dot{x}_r\right)\right] \tag{9}$$

where $\hat{F} = U^2\left(ax^2 + bx + c\right)$. Therefore, the equivalent control input U_{eq}^2 can be expressed as

$$U_{eq}^2 = \frac{\hat{F}}{ax^2 + bx + c}. \tag{10}$$

The summation of U_{eq}^2 and a basic switching function U_s forms the overall control law for the EERLSMC, where the switching function be defined as follows:

$$U_S = \frac{U_R}{ax^2 + bx + c}. \tag{11}$$

Then, the overall control law U_C^2 can be obtained by adding (10) and (11) together to ensure that the DEA always stays on the sliding surface with finite convergence time. Thus, U_C^2 can be expressed as

$$U_C^2 = \frac{\hat{F} + U_R}{(ax^2 + bx + c)} \tag{12}$$

where U_R is the enhanced exponential reaching law that can drastically reduce chattering effects. It achieves this by utilizing a saturation function of relatively high gradient and includes the advantages of an exponential function and a power term to guarantee finite time convergence. Thus, U_R employed in this work is given as

$$\dot{\delta} = U_R = -\left[K_1\delta + \frac{K_2|\delta|^{\gamma}}{\alpha + (1-\alpha)\, e^{-\beta|\delta|}}\text{sat}\left(\frac{\delta}{\omega}\right)\right] \tag{13}$$

where sat is the saturation function. ω in the saturation function is chosen to be much smaller than $|\delta|$ to provide a high gradient. The term $K_1\delta$ enhances faster convergence ($K_1 > 0$) by accelerating its dynamic responses. Saturation function (for $\omega \ll |\delta|$) with the exponential function $e^{-\beta|\delta|}$ at the denominator guarantees finite time convergence and the smoothness of the control input signal. The term $K_2|\delta|^{\gamma}$, in conjunction with α and set value of ω and K_1, controls chattering excitation and adjusts the reaching time to approach the sliding surface. Before we test the performance of the EERLSMC, we need to prove its stability and robustness in the following section at first.

B. Controller Stability and Robustness Analysis

Proposition 1: Combining with the generalized dynamic model given in (4), the overall EERLSMC's control law given by (12) relates to the sliding equivalent control law U_{eq}^2 of (10), the force input (9), and the sliding hyperplane function based on the reaching law in (13). In addition, recognizing the presence of model uncertainty, environmental factors, and random disturbances, we introduce a bounded disturbance term ψ into the control law. This inclusion serves the purpose of conducting robustness analysis to account for modeling errors arising from these sources. According to the overall control law and the defined sliding surface, the system will be stable and robust if the condition specified by the Lyapunov candidate holds.

Proof: From the overall system control law, which can be fully expressed as

$$\begin{aligned} U_C^2 = \Bigg\{ & \eta_0\dot{x} + px + qx^2 + \sum_{i=1}^{n} k_i z_i + m\ddot{x}_r - m\frac{\lambda}{\xi}\left(\dot{x} - \dot{x}_r\right) \\ & + \psi - \left[K_1\delta + \frac{K_2|\delta|^{\gamma}}{\alpha + (1-\alpha)\, e^{-\beta|\delta|}}\text{sat} \right. \\ & \left. \times \left(\frac{\delta}{\omega}\right)\right] \Bigg\}\left(ax^2 + bx + c\right)^{-1}. \end{aligned} \tag{14}$$

It is obvious from (14) that the system stability can be validated through the reaching law as it directly relates to the sliding manifold upon which the system stability depends, this will be shown later.

Hence, to prove the controller stability, we defined a Lyapunov candidate function $V(\delta) : \Re \to \Re$, such that

$$V(\delta) = 0.5\delta^2 \tag{15}$$

with following constraints:

$$\begin{cases} V(\delta) \geq 0 & \forall\delta \in R \\ V(\delta) = 0 & \delta = 0 \\ \dot{V}(\delta) < 0 & \delta \neq 0. \end{cases} \tag{16}$$

The first two constraints are directly satisfied by the chosen candidate, since (15) will be greater than zero for all real values of the sliding manifold and will be zero if and only if the sliding manifold is zero. But the controllers stability will be guaranteed if the third constraint is appropriately satisfied.

To validate this, (15) is differentiated with respect to time, which yields

$$\dot{V}(\delta) = \delta\dot{\delta}. \tag{17}$$

Putting (8) into (17) yields

$$\dot{V}(\delta) = \delta\left[\xi\left(\ddot{x} - \ddot{x}_r\right) + \lambda\left(\dot{x} - \dot{x}_r\right)\right]. \tag{18}$$

Combining with the overall control law given by (14) and generalized dynamic model in (4), (18) becomes

$$\dot{V}(\delta) = -\frac{\delta\xi}{m}\left[K_1\delta + \frac{K_2|\delta|^{\gamma}}{\alpha + (1-\alpha)\, e^{-\beta|\delta|}}\text{sat}\left(\frac{\delta}{\omega}\right) - \psi\right]. \tag{19}$$

Equation (19) clearly indicates that the system stability depends on the switching function. Thus, (19) can be further simplified as

$$\dot{V}(\delta) = -\frac{\xi}{m}\left[K_1\delta^2 + \frac{K_2|\delta|^{\gamma}\delta}{\alpha + (1-\alpha)\, e^{-\beta|\delta|}}\text{sat}\left(\frac{\delta}{\omega}\right) - \psi\delta\right]. \tag{20}$$

The high gradient saturation function, $\text{sat}(\frac{\delta}{\omega})$ is defined as

$$\text{sat}\left(\frac{\delta}{\omega}\right) = \begin{cases} \frac{\delta}{\omega} & \left|\frac{\delta}{\omega}\right| \leq 1 \\ \text{sgn}\left(\frac{\delta}{\omega}\right) & \left|\frac{\delta}{\omega}\right| > 1. \end{cases} \tag{21}$$

As ω approaches zero, $|\delta/\omega| > 1$ and $\text{sat}(\delta/\omega) \equiv \text{sgn}(\delta/\omega) = |\delta|/\delta$. From the identity, (20) can be rewritten as

$$\dot{V}(\delta) = \begin{cases} -\frac{\xi}{m}\left[K_1\delta^2 + \frac{K_2|\delta|^{\gamma+2}}{\left[\alpha+(1-\alpha)e^{-\beta|\delta|}\right]\omega} - \psi\delta\right] & \left|\frac{\delta}{\omega}\right| \le 1 \\ -\frac{\xi}{m}\left[K_1\delta^2 + \frac{K_2|\delta|^{\gamma+1}}{\alpha+(1-\alpha)e^{-\beta|\delta|}} - \psi\delta\right] & \left|\frac{\delta}{\omega}\right| > 1. \end{cases} \tag{22}$$

From (22), by choosing $\{\xi, \lambda, \alpha, \beta, \gamma, \omega\} \in R_+$ and $K_1, K_2 > \psi$, the sliding manifold will approach the equilibrium point, as $\dot{V}(\delta)$ will not be zero. Thus, the stability and robustness of the system are guaranteed, since $\dot{V}(\delta) < 0$, for $\delta^2 > 0$, $|\delta| > 0$, (i.e., : $\delta \neq 0$) and $\varphi_s > \varphi_d$, where $\varphi_s = K_1\delta^2 + \frac{K_2|\delta|^{\gamma+1}}{\alpha+(1-\alpha)e^{-\beta|\delta|}}$ and $\varphi_d = \psi\delta$. In real-time implementation, the $sat(\delta/\omega)$ is used to wind-up the chattering effect posed by the discontinuous function $\text{sgn}(\delta/\omega)$.

C. Convergence Time Analysis

Proposition 2: For the system reaching law given by (13), the system as proved by (22) converges to equilibrium (stable), as it approaches the sliding hyperplane at finite time T_R.

Proof: To evaluate the reaching time T_R, the first term in the (13) is ignored, hence the reaching law can be expressed as

$$\dot{\delta} = -\frac{K_2|\delta|^{\gamma}}{\alpha + (1-\alpha)\, e^{-\beta|\delta|}} \text{sat}\left(\frac{\delta}{\omega}\right). \tag{23}$$

Since, $\text{sat}\left(\frac{\delta}{\omega}\right) \to \text{sgn}(\delta)$ as $\omega \to 0$, then (23) can be rewritten as

$$\dot{\delta} = -\frac{K_2|\delta|^{\gamma}}{\alpha + (1-\alpha)\, e^{-\beta|\delta|}} \text{sgn}(\delta). \tag{24}$$

Initially, the sliding manifold δ does not equal to zero (i.e., : $\delta \neq 0$). It starts from a given initial value δ_0 and is constrained according to the design to converge to zero (i.e., : $\delta = 0$). Based on (24), the convergence (reaching) time can be obtained as follows:

$$\frac{d\delta}{dt} = -\frac{K_2|\delta|^{\gamma}}{\alpha + (1-\alpha)\, e^{-\beta|\delta|}} \text{sgn}(\delta)$$

$$\Rightarrow -K_2 dt = \frac{\alpha + (1-\alpha)\, e^{-\beta|\delta|}}{|\delta|^{\gamma}\text{sgn}(\delta)} d\delta. \tag{25}$$

Taking the definite integration of (25) between zero and T_R leads to (note: $\delta(T_R) = 0$)

$$-\int_0^{T_R} K_2 dt = \int_{\delta_0(t=0)}^{\delta(T_R)} \frac{\alpha + (1-\alpha)\, e^{-\beta|\delta|}}{|\delta|^{\gamma}\text{sgn}(\delta)} d\delta \tag{26}$$

By solving (26), we can get

$$T_R = \frac{|\delta_0|^{1-\gamma}\left[\alpha + (1-\alpha)\, e^{-\beta|\delta_0|}\right]}{K_2(1-\gamma)}. \tag{27}$$

The resulting T_R in (27) holds for $\Re(|\delta_0|) \ge 0$ and $\Re(\gamma) < 1$. It is worth noting that the initial first term ignored in (13) can further accelerate the dynamic convergence response of the controller. Thus, the controller dynamic convergence response (reaching time) will be lesser than that resulting from (27).

TABLE I
IDENTIFIED PARAMETERS OF DYNAMIC MODELS FOR FOUR DEAS

DEA	Planar	Conical	DEA-MES	2DOF-DEA-X	2DOF-DEA-Y
m/kg	0.0164	0.30	0.023	0.026	0.026
a	2.93	0	1.43	0.31	3.07
b	0.0018	0.001	0.0016	0.30	0.29
c	0.0106	0.032	0.031	0.017	0.015
p	431.27	325.64	81.86	112.65	101.00
q	184.51	0.055	26.76	5.87	5.39
η_0	0.0038	0.041	0.021	2.48	2.43
k_1	93.22	129.67	2579.35	325.80	296.34
k_2	29.75	238.15	103.54	66.83	62.44
k_3	68.81	15.42	32.22	35.19	31.85
k_4	0.115	0.63	0.011	0.011	0.011
η_1	0.684	0.46	2.12	7.18	6.40
η_2	5.68	7.24	5.05	36.39	35.48
η_3	12.81	13.41	58.44	342.76	325.32
η_4	702.60	148.27	378.20	2097.28	1961.49

D. Convergence of the State Observer

Proposition 3: For the state observer in Fig. 3, it will be stable and convergent if all the parameters of the rheological units are larger than zero.

Proof: Based on the Lyapunov stability theory, we select the Lyapunov function candidate as

$$V(z_i) = \frac{1}{2}\left(z_i - \frac{\eta_i}{k_i}\dot{x}\right)^2. \tag{28}$$

The derivative of (28) can be expressed as

$$\dot{V}(z_i) = \left(z_i - \frac{\eta_i}{k_i}\dot{x}\right)\dot{z}_i. \tag{29}$$

Combining with $k_i z_i = \eta_i(\dot{x} - \dot{z}_i)$, the (29) can be written as

$$\dot{V}(z_i) = -\frac{k_i}{\eta_i}\left(z_i - \frac{\eta_i}{k_i}\dot{x}\right)^2. \tag{30}$$

Based on the identified parameters in Table I, $\frac{k_i}{\eta_i}$ is always positive for all DEAs. Thus, $\dot{V}(z_i) < 0$ for all $z_i \neq \frac{\eta_i}{k_i}\dot{x}$, indicating a negative semidefinite $\dot{V}(z_i)$. Then, for $\dot{V}(z_i) < 0$, $V(z_i)$ will decrease, subsequently the state observer discrepancy between the predicted state $\dot{z}_i$ and the true $\dot{x}$ converges to zero for all $t > 0$, hence proving the state observer stability. Similarly, except for $z_i = \frac{\eta_i}{k_i}\dot{x}$, the Lyapunov function is strictly decreasing. This shows that z_i converges to $\frac{\eta_i}{k_i}\dot{x}$, proving the state observer's convergence.

IV. EXPERIMENTAL VALIDATION

Based on above analysis, we can see that the EERLSMC is mathematically stable, which paves the way for the application

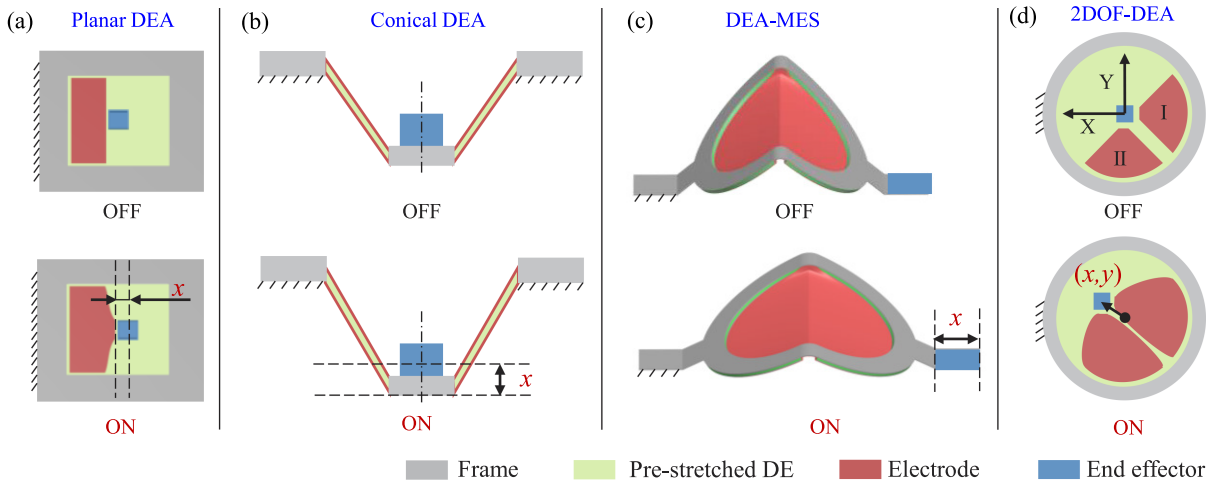

Fig. 4. Structure and working principle of four types of DEAs. (a) Planar DEA. (b) Conical DEA. (c) DEA-MES; (d) 2DOF-DEA.

of the EERLSMC in the field of DEAs. Further, different experiments are conducted to verify the effectiveness of the generalized dynamic model and EERLSMC.

A. *DEAs for Proof-Concept-Testing*

In previous work, many DEAs with different configurations and materials have been developed to generate different actuation. To verify the generality, both configurations, materials, and DOFs need to be taken into account. For the configuration, it mainly determines the geometric shapes, such as planar, conical, and minimum energy structure. The mostly used materials includes the silicone and acrylic elastomer. The silicone elastomer demonstrates less viscoelasticity while the acrylic elastomer can generate larger deformation. Without loss of generality, we adopt four kinds of DEAs (see Fig. 4), including planar DEA [28] (Case I, made of silicone elastomer), conical DEA [13] (Case II, made of acrylic elastomer), DEA-MES [30] (Case III, made of acrylic elastomer), and 2DOF-DEA [35], [36] (Case IV, made of acrylic elastomer) for proof-of-concept testing. The main structure and working principle of them are detailed in the following.

Case I. Planar DEA: It mainly consists of a prestretched silicone elastomer membrane (Wacker ELASTOSIL Film 2030, initial thickness 0.1 mm, prestretched ratio 1.5) that is fixed on a stiff frame made of a laser-cut polymethyl methacrylate board (thickness 3 mm). A baffle is adhered to the middle of the planar DEA, which separates the silicone elastomer membrane into active and passive regions. The active region is coated on both sides with compliant electrodes (Carbon grease, MG Chemical 846–80G) while the passive region is working as a passive spring. When a high voltage is applied to the active region, the Maxwell stress leads to expand of the active region and shrink of the passive region, generating a 1-DOF planar actuation, shown in Fig. 4(a).

Case II. Conical DEA: It mainly composes of an acrylic elastomer membrane (3 M VHB 4910, initial thickness 1 mm) with a prestretch ratio of 3 that is supported by a stiff frame.

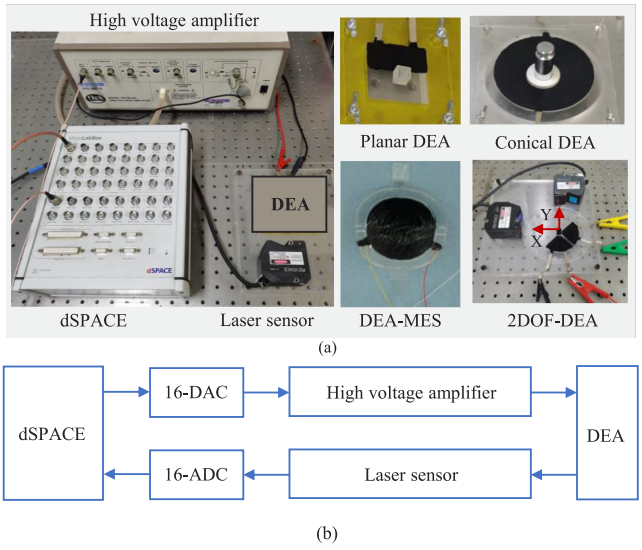

Fig. 5. Experimental setup. (a) Experimental equipment and four DEAs used in this work. (b) Block diagram representation.

An inner stiff disk is adhered to the center of the prestretched acrylic elastomer membrane, which is used to connect with the end-effector (a mass with a weight of 100 g in this work). Carbon grease (MG Chemical 846–80G) working as complaint electrode is used to coat on both sides of the acrylic elastomer membrane. When a high voltage is applied, the conical DEA generates a 1-DOF vertical displacement due to the expand of the acrylic elastomer membrane, shown in Fig. 4(b).

Case III. DEA-MES: It consists of a prestretched acrylic elastomer membrane (3 M VHB 4910, initial thickness 1, prestretched ratio 5) that is adhered to a flexible frame. Carbon grease (MG Chemical 846–80G) working as compliant electrodes is used to coated on both sides of the acrylic elastomer membrane. When the prestretch is released, the prestretched stress within the acrylic elastomer membrane leads to bending of the flexible frame until the stress of the acrylic elastomer membrane balances with the restoring force of the flexible frame,

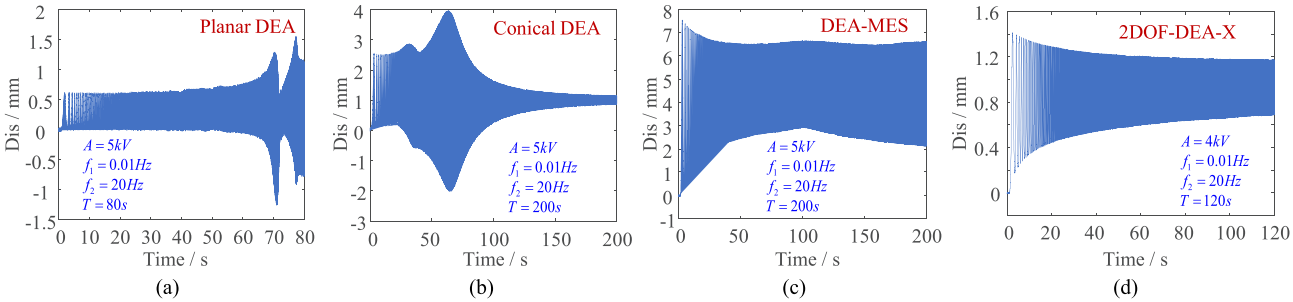

Fig. 6. Sweep-frequency tests of four DEAs. (a) Planar DEA. (b) Conical DEA. (c) DEA-MES. (d) 2DOF-DEA.

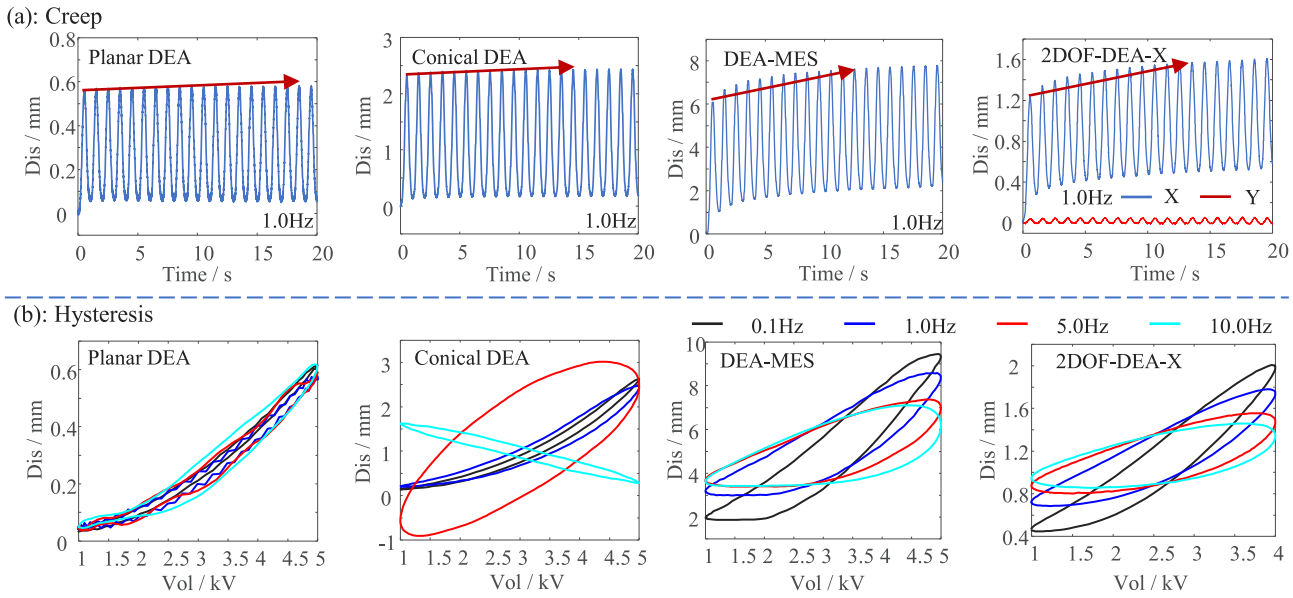

Fig. 7. Dynamic responses of the four DEAs under sinusoidal excitation voltages. (a) Slow-time creep phenomenon. (b) Rate-dependent hysteresis nonlinearity coupled with the mechanical vibration.

forming a saddle shape (called minimum energy structure). When a high voltage is applied, the expansion of the acrylic elastomer membrane leads to extension of the flexible frame that is converted into a 1-DOF movement by two flexible joints, shown in Fig. 4(c).

Case IV. 2DOF-DEA: It consists of a prestretched acrylic elastomer membrane (3 M VHB 4910, initial thickness 1, prestretched ratio 3) that is adhered to a stiff frame (inner diameter 90 mm and outer diameter 120 mm). Two pairs (I and II) of fan-shaped compliant electrodes (made of carbon grease, MG Chemical 846–80G) are fabricated. The elastomer membrane without electrode is working as passive nonlinear spring. A cubic end effector is adhered to the center of the dielectric elastomer membrane. When voltages are applied to electrode I and electrode II, it can generate a 2-DOF (named as 2DOF-DEA-X and 2DOF-DEA-Y) actuation in the XY plane, shown in Fig. 4(d).

B. System Description and Experimental Method

In order to characterize the dynamic responses of above DEAs and verify our generalized motion control framework, we establish an experimental setup, shown in Fig. 5. The experimental setup mainly consists of two high voltage amplifiers (Trek 10/10B-HS), two laser sensors (Keyence LK-H085), a control module (dSPACE Microlab 1202) and DEAs. The high voltage amplifiers with a gain of 1000 is utilized to provide excitation voltage for DEAs. The laser sensors can capture the output displacement and convert it (in the range of $-20\sim20$ mm) into analog signal (in the range of $-10\sim10$ V). The control module with 16-b analog-to-digital converter (16-ADC) and 16-b digital-to-analog converter (16-DAC) is used to generate control signal for the high voltage amplifiers and record the displacement from the laser sensors. The sampling time is set as 1 ms in this work. We should mention that only the 2DOF-DEA needs two high voltage amplifiers and two laser sensors. Considering that their breakdown voltages, the amplitude of the excitation voltage of planar DEA, conical DEA and DEA-MES is limited to 5 kV while that of 2DOF-DEA is set as 4 kV during the following experiments. Based on the experimental setup, we would like to first illustrate the experimental process and then demonstrate the experimental results and verification. The experimental process mainly involves the following three steps.

1) Characterization of dynamic responses: We first conduct a sweep frequency test to reveal the amplitude-frequency response of DEAs. The excitation voltage V_{sweep} (in kV) can be expressed as

$$V_{\text{sweep}} = A_1 \sin\left[\pi t\left(\frac{f_2 - f_1}{T}t + f_1\right) - \frac{\pi}{2}\right] + A_2 \quad (31)$$

where t represents the time. The frequency is in the range of f_1 and f_2. T represents the lasting time of the sweep frequency test. A_1 and A_2 represent the amplitude and offset of the sweep excitation voltage, respectively. For the planar DEA, conical DEA and DEA-MES, A_1 and A_2 are set as 2 and 3, respectively. For the 2DOF-DEA, A_1 and A_2 are selected as 2. Then, in order to investigate the viscoelasticity and mechanical vibration of DEAs, we measure the dynamic responses under sinusoidal voltages V_{sin} (in kV) with different frequency that can be written as

$$V_{\text{sin}} = B_1 \sin(2\pi f t - \pi/2) + B_2 \quad (32)$$

where f, B_1, and B_2 represent the frequency, amplitude, and offset of the excitation voltage, respectively. For the planar DEA, conical DEA, and DEA-MES, B_1 and B_2 are set as 2 and 3, respectively. For the 2DOF-DEA, B_1 and B_2 are selected as 1.5 and 2.5, respectively. Lastly, we analyze the influence of viscoelasticity and mechanical vibration on the dynamic responses of DEAs.

2) Dynamic modeling: Based on above experimental data, the unknown parameters in the generalized dynamic model (4) are identified. To this end, we first need to select the number of rheological units in (4). Based on our experience, four rheological units are enough to describe the viscoelasticity of DEAs. Further increasing the number of rheological units may not improve the accuracy of the dynamic model but cause computational difficulty. Then, we define a loss function as optimization object that can be expressed as

$$J = \sum_{j=1}^{M} (y_{jE} - y_{jP})^2 \quad (33)$$

where M represents the number of the experimental data used for identification. y_{jE} and y_{jP} represent the experimental data and predicted results with the jth frequency. Lastly, a Bayesian optimization-based parameters identification method [28] is adopted to identify those unknown parameters and the effectiveness of the dynamic model is validated by comparing the experimental data with predicted results.

3) EERLSMC verification: Combining with the identified dynamic model, the EERLSMC is first established and controller parameters are selected based on a trial-and-error method. Then, sinusoidal trajectory tracking experiments are conducted under different frequencies, which can be expressed as

$$D_s(t) = C_1 \sin\left(2\pi f t - \frac{\pi}{2}\right) + C_2 \quad (34)$$

where f, C_1, and C_2 represent the frequency, amplitude, and offset of the sinusoidal trajectory, respectively. The experimental results are used to verify the effectiveness of the EERLSMC for removing the rate-dependent viscoelasticity. Lastly, more complex trajectories (such as triangle wave and sinusoidal trajectory with changing amplitude and frequency) are used to further validate the controller.

TABLE II
PREDICTED ERRORS UNDER DIFFERENT FREQUENCIES

DEA	Planar		Conical		DEA-MES		2DOF-DEA-X		2DOF-DEA-Y	
Fre/Hz	e_m	e_{rms}	e_m	e_{rms}	e_m	e_{rms}	e_m	e_{rms}	e_m	e_{rms}
0.1	6.05	2.98	7.98	3.32	14.88	6.07	7.60	4.27	8.34	4.23
1.0	10.72	2.98	9.08	3.67	11.54	4.17	9.73	5.33	11.67	6.35
5.0	10.71	4.13	6.34	2.96	12.10	5.66	6.79	2.40	6.81	2.34
10.0	17.75	5.97	14.78	7.60	15.81	9.42	5.49	3.07	5.10	2.63

e_m/e_{rms} : %

C. Experimental Results

Based on above experimental processes, experimental results of four kinds of DEAs are illustrated in the following. Fig. 6 shows the amplitude–frequency responses of four DEAs. It can be seen as follows.

1) For the planar DEA, the amplitude is almost constant under relative low frequency and then become complex [see Fig. 6(a)].
2) The conical DEA contains two obvious resonant frequencies [about 3.0 and 6.0 Hz, Fig. 6(b)].
3) The amplitude of the DEA-MES also relies on the frequency, but there is no obvious resonance [see Fig. 6(c)].
4) The amplitude of the 2DOF-DEA-X rapidly decreases with the increase of frequency without resonance.

Therefore, the dynamic responses of DEAs highly depend on the configuration and the excitation frequency. Further, Fig. 7 shows the dynamic responses of four DEAs under sinusoidal excitation voltages, which demonstrate the following.

1) The time-domain experimental results show a slow drift phenomenon due to the creep nonlinearity [see Fig. 7(a)].
2) For the 2DOF-DEA, although the sinusoidal excitation voltage is only applied to one axis, the other axis still generates a periodic movement with a small amplitude, due to cross-coupling [see Fig. 7(a)].
3) There is obvious hysteresis nonlinearity that is asymmetric and rate-dependent [see Fig. 7(b)].

It should be noted that two axes of the 2DOF-DEA show very similar dynamic characteristics. Consequently, Figs. 6 and 7 only show the experimental data of the *X*-axis. To fully describe the complex dynamic responses, our generalized dynamic model needs to self-adapt the configuration, material and frequency of DEAs.

Remark: In our earlier study [13], we presented plots of the output displacement as a function of the squared voltage. These plots illustrated that the hysteresis loops remain asymmetric and rate-dependent. Consequently, the nonlinearity between

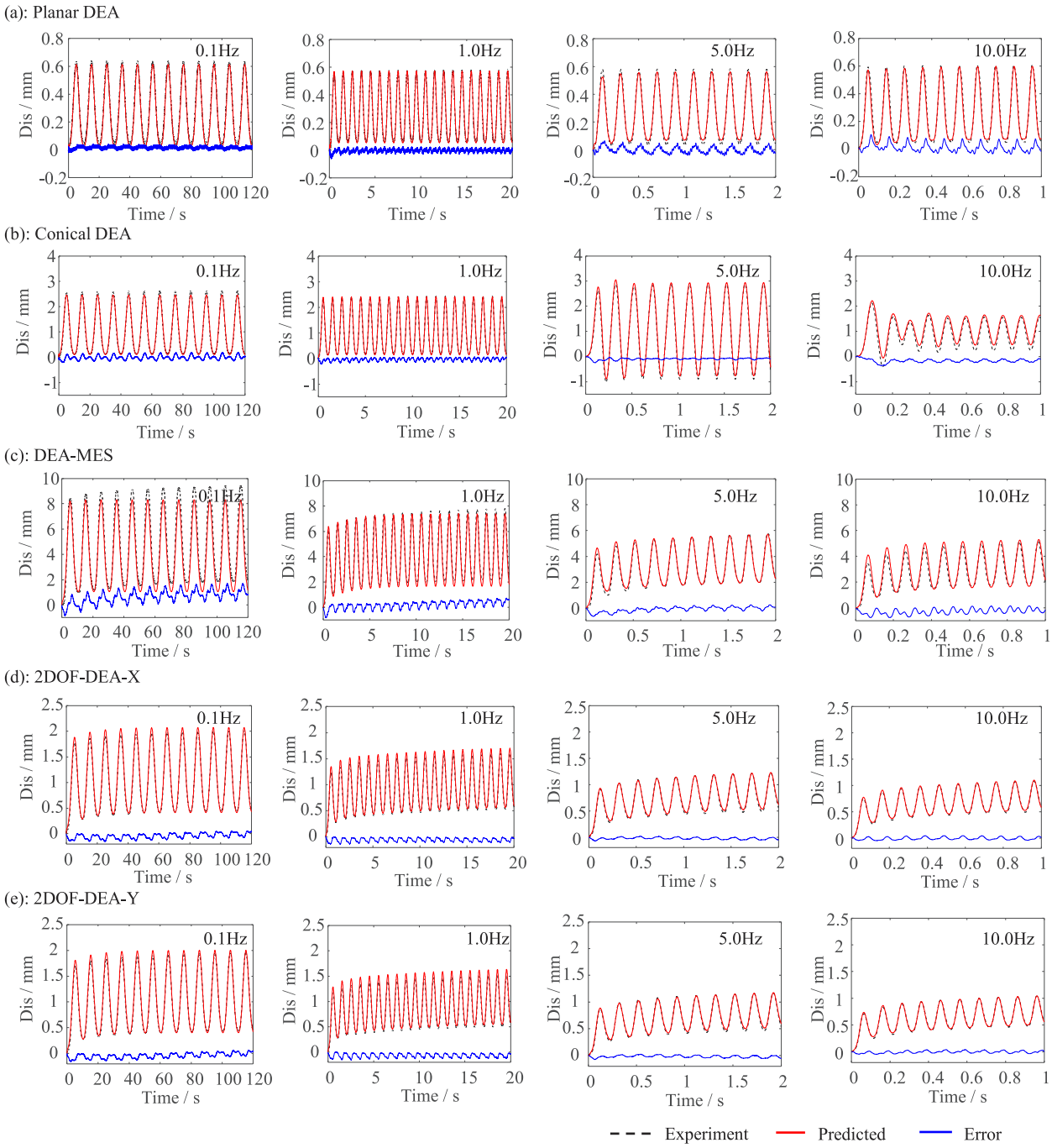

Fig. 8. Comparisons between the experimental data and predicted results of the generalized dynamic model. (a) Planar DEA. (b) Conical DEA. (c) DEA-MES. (d) 2DOF-DEA-X. (e) 2DOF-DEA-Y.

TABLE III
CONTROL PARAMETERS IN THE EERLSMC FOR FOUR DEAS

Parameter	λ	K_1	K_2	β	ω	ξ	γ	α
Planar	1.8	1	0.35	20	0.00115	1	0.01	1.85
Conical	2	0.1	0.5	1.5	0.0004	0.05	0.05	0.25
DEA-MES	12	2	0.34	20	0.0045	1	0.01	2
2DOF-DEA-X	1.5	110	0.5	1.5	0.00045	0.1	0.09	0.5
2DOF-DEA-Y	1.6	130	0.5	1.5	0.00065	0.1	0.09	0.5

the output displacement and voltage is not solely attributed to the nonlinear Maxwell stress but also depends on material nonlinearity, encompassing hyperelasticity and viscoelasticity. In addition, the resonance highly relies on the configurations and materials of DEAs. In this work, we mainly focus on modeling and eliminating the complex dynamic responses of DEAs. The influence of configurations, materials and dimensions on the resonance may be out the scope of this work, which may be investigated in the future work.

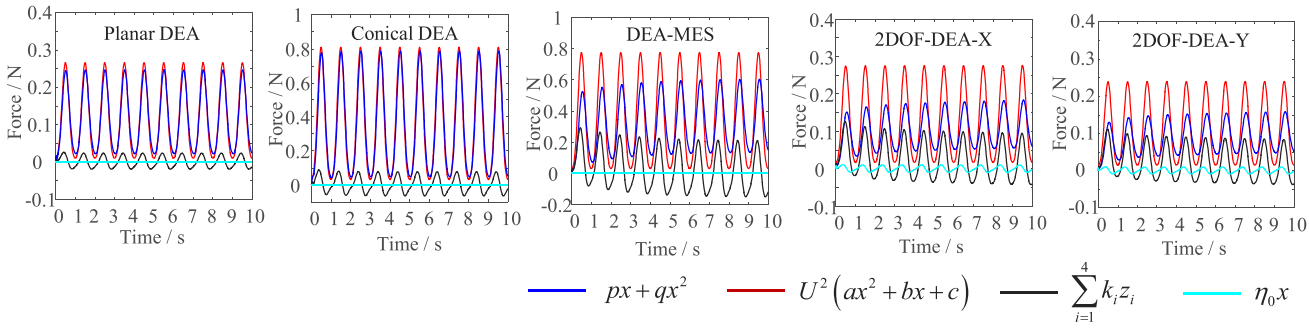

Fig. 9. Elastic force, actuation force, viscoelastic force, and structural damping are plotted as a function of time when the four DEAs are actuated by a sinusoidal voltage with a frequency of 1.0 Hz.

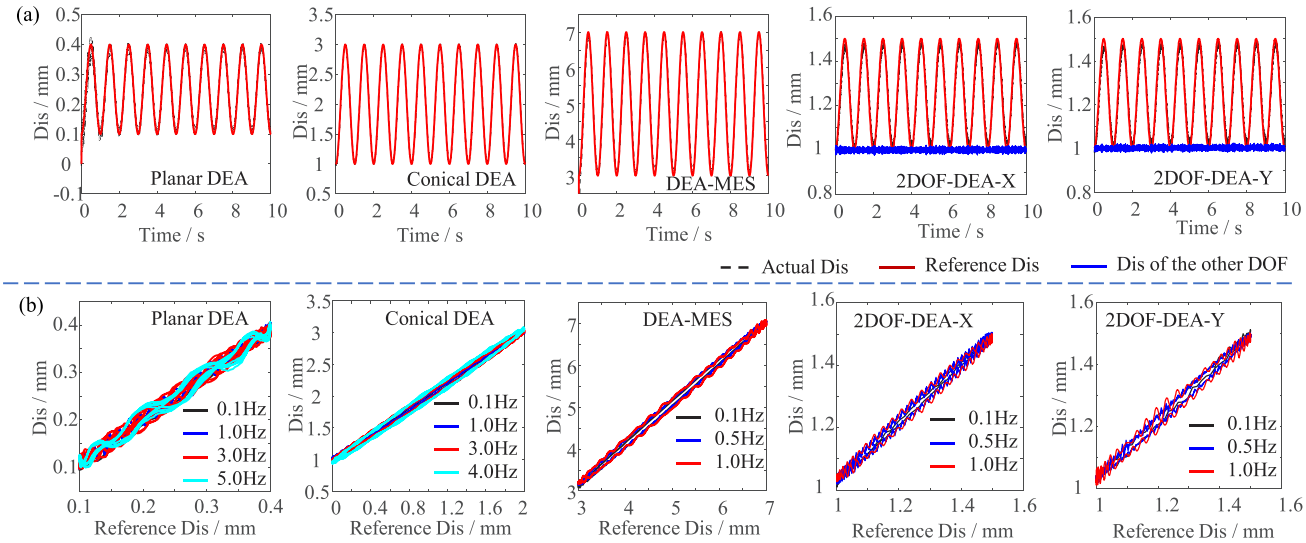

Fig. 10. Experimental results of tracking sinusoidal trajectories under different frequencies. (a) Time-domain comparison of output displacement and the reference displacement. (b) Output displacements are plotted as a function of reference displacements.

TABLE IV
TRACKING ERRORS OF THREE DEAS UNDER DIFFERENT FREQUENCIES

Planar DEA	No controller		EERLSMC		Conical DEA	No controller		EERLSMC		DEA-MES	No controller		EERLSMC	
Fre	e_m	e_{rms}	e_m	e_{rms}	Fre	e_m	e_{rms}	e_m	e_{rms}	Fre	e_m	e_{rms}	e_m	e_{rms}
0.1	20.36	10.03	8.84	3.44	0.1	26.99	14.44	2.59	0.84	0.1	33.11	14.65	4.41	2.51
1.0	27.82	14.95	10.00	4.03	1.0	32.99	16.90	3.82	1.44	0.5	45.76	23.89	4.83	2.37
3.0	26.78	14.49	17.92	6.67	3.0	52.82	24.42	6.95	2.82	1.0	49.36	26.44	5.29	2.86
5.0	29.36	14.75	25.69	9.16	4.0	36.06	24.56	8.67	3.87	2.0	57.17	31.87	22.78	8.75

Fre: Hz e_m/e_{rms} : %

TABLE V
TRACKING ERRORS AND CROSS-COUPLING ERRORS OF THE 2DOF-DEA UNDER DIFFERENT FREQUENCIES

X	No controller				EERLSMC				Y	No controller				EERLSMC			
Fre	e_m	e_{rms}	C_m	C_{rms}	e_m	e_{rms}	C_m	C_{rms}	Fre	e_m	e_{rms}	C_m	C_{rms}	e_m	e_{rms}	C_m	C_{rms}
0.1	29.69	13.74	80	37	8.53	3.29	26	10	0.1	31.14	14.54	64	28	9.82	3.37	39	15
0.5	40.57	21.91	53	25	9.18	4.29	22	10	0.5	42.31	23.11	33	15	9.66	4.38	28	10
1	48.19	27.59	50	24	10.77	5.24	22	9	1	50.16	29.15	39	17	11.72	5.49	23	9
2	54.69	30.93	45	24	12.14	6.78	24	9	2	56.05	32.00	24	10	14.67	7.30	19	9

Fre: Hz e_m/e_{rms} : % C_m/C_{rms} : um

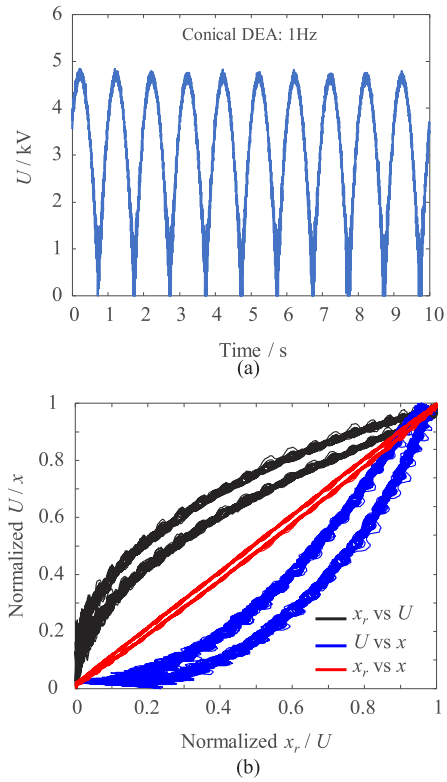

Fig. 11. One example of the signal flow within the EERLSMC when the conical DEA is used to track a sinusoidal trajectory (1 Hz). (a) Actual excitation voltage U. (b) Relationship between the normalized x_r, U, and x.

Based on recorded experimental data presented here, our generalized dynamic model is employed and its unknown parameters are identified and listed in Table I. Fig. 8 also shows the comparison between experimental data and predicted results. To quantitatively describe the predicted errors, we further define two errors, including max errors e_m and root-mean-square error e_{rms}, as

$$e_m = \frac{\max|y_E - y_P|}{\max(y_E) - \min(y_E)} \times 100\%$$
$$e_{rms} = \frac{\sqrt{\frac{1}{N}\sum_{i=1}^{N}(y_E - y_P)^2}}{\max(y_E) - \min(y_E)} \times 100\% \quad (35)$$

where y_E and y_P represent the experimental data and predicted results, respectively. N is the length of y_E or y_P. Based on the definition, we can evaluate the e_m and e_{rms} under different frequencies, listed in Table II. When the frequency is in the range of 0.01–10.0 Hz, their e_m are 17.75%, 14.78%, 15.81%, 9.73%, and 11.67%, respectively, and their e_{rms} are limited to 5.97%, 7.60%, 9.42%, 5.33%, and 6.35%, respectively. It clearly demonstrates that our dynamic model can precisely describe the complex dynamic responses (including rate-dependent viscoelasticity, mechanical vibration, and their coupling) of DEAs with different configurations, materials and DOFs, verifying the generality and versatility of our dynamic model. In addition, based on the identified parameters in Table I, we further quantify the role of each component in the dynamic model (4). When the four DEAs are actuated by a sinusoidal voltage (1 Hz as an example), the elastic force, actuation force, viscoelastic force, and structural damping are plotted as a function of time (see Fig. 9). It can be seen that the elastic force, actuation force, and viscoelastic force are at the same level and dominate the dynamic responses of the DEAs together. Especially, the unignorable viscoelastic force leads to rate-dependent hysteresis nonlinearity that cannot be eliminated by state feedback controllers [13].

We should mention that although the purely phenomenological models also can be used to describe the rate-dependent viscoelasticity of different DEAs, they usually can not characterize the mechanical vibration due to the absence of mechanic structure in the models, limiting their applications. Therefore, the main advantage of our generalized dynamic model includes the following.

1) Different from existed physical models, our generalized dynamic model not only contains lesser parameters and possesses a simpler structure, but also shows the versatility to accommodate different configurations, materials and DOFs.
2) Comparing with phenomenological models, our generalized dynamic model takes both the mechanical structure and viscoelasticity into account, which can historically characterize the complex dynamic responses of DEAs.
3) It is one kind of control-enabling models, which can be used for controller design and stability analysis.

Based on the generalized dynamic model, we further establish the EERLSMC for four DEAs. The selected controller parameters of each DEA are listed in Table III. Fig. 10 shows the comparison between the actual displacement and the reference displacement under different frequencies. In order to evaluate the performance of the EERLSMC, we further characterize the e_m and e_{rms} when no controller is applied. However, we cannot directly compute them because the dimension of the voltage and displacement shown in Fig. 8 is different. Therefore, we first normalize all displacement based on the maximum and minimum displacement of the experimental results when the frequency equals 0.1 Hz. Then, the voltages are normalized based on the maximum and minimum voltage. With the normalized experimental data, we can obtain e_m and e_{rms} based on (32). The results of the Planar DEA, Conical DEA, and DEA-MES are listed in Table IV. To characterize the cross-coupling effect of the 2DOF-DEA, we further define two cross-coupling errors C_m and C_{rms} as

$$C_m = \max|D_c - D_r|$$
$$C_{rms} = \sqrt{\frac{1}{N}\sum(D_c - D_r)^2} \quad (36)$$

where D_c represents the actual displacement caused by the cross-coupling effect. D_r is the reference displacement that equals 0 in Fig. 8 and 1 mm in Fig. 10. Based on above definition, all errors of the 2DOF-DEA are illustrated in Table V.

It can be seen that with the EERLSMC, all DEAs can achieve high-precision tracking control by eliminating the creep, rate-dependent hysteresis and mechanical vibration within a

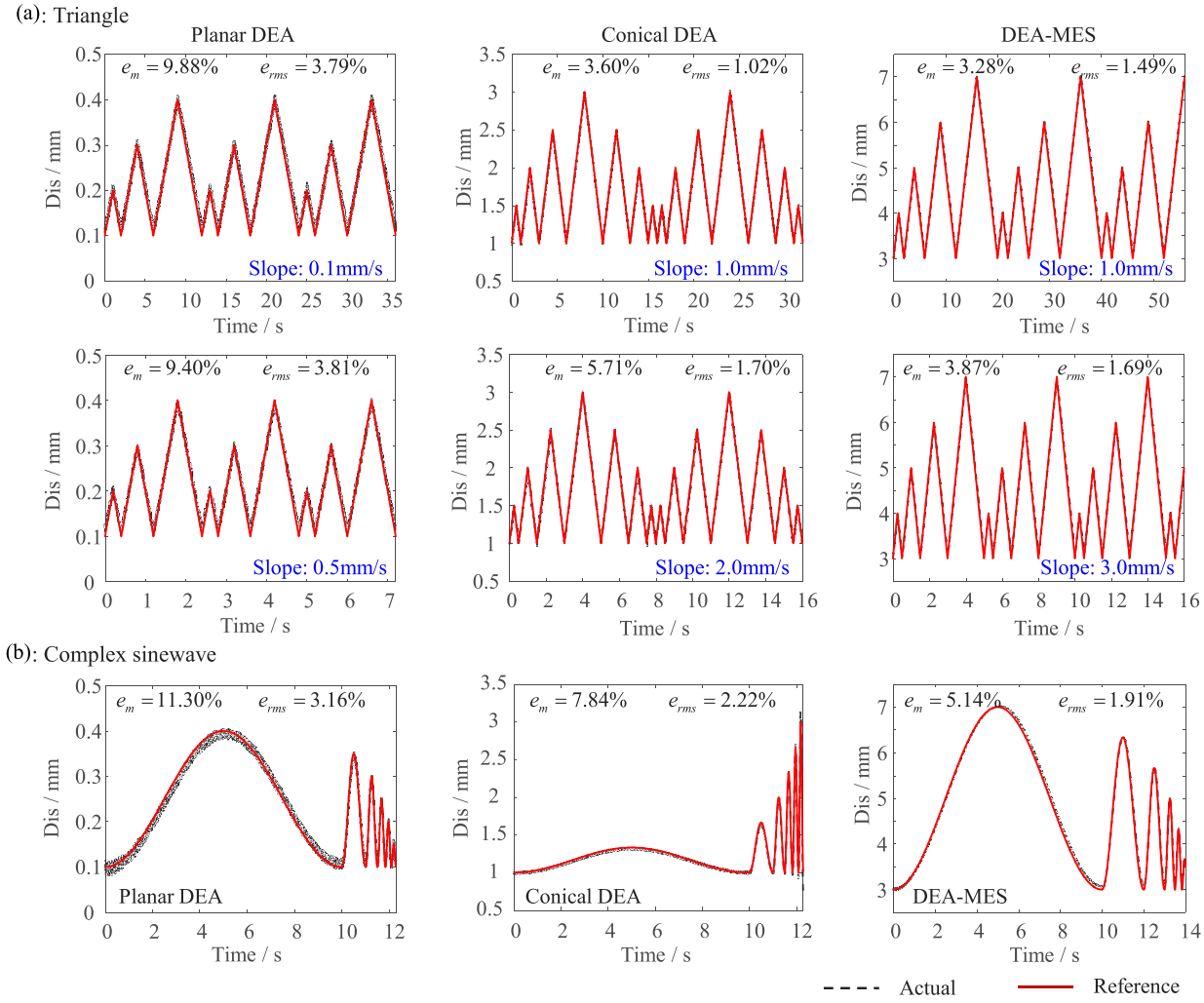

Fig. 12. Experimental results of tracking complex trajectories. (a) Tracking triangle trajectories with different slopes and amplitudes. (b) Tracking sinusoidal trajectories with changing frequency and amplitude.

certain frequency range. The e_{rms} of four DEAs are less than 10%. In the meantime, the cross-coupling effect of the 2DOF-DEA is also minimized by the EERLSMC. Both C_m and C_{rms} are decreased by more than 50%. The above experimental results demonstrate that the EERLSMC can also self-adapt DEAs with different configurations, materials and DOFs. The main reason depends on the fact that the EERLSMC is one kind of model-based controllers. As a result, the designed EERLSMC contains the dynamic features of the DEAs, enhancing the capability of generality, robustness and ease of use. We also notice that the working frequency of the EERLSMC (4.0 Hz) for the conical DEA is larger than its first resonant frequency [about 3.0 Hz, shown in Fig. 6(b)]. It demonstrates that the EERLSMC shows the ability to eliminate the mechanical vibrations of DEAs, overcoming the drawback of traditional feedforward plus feedback controllers [13], [19] whose working frequency is generally much less than their resonant frequency.

In addition, to understand clearly why the EERLSMC can achieve high-precision tracking control of DEAs, one example of the signal flow within the EERLSMC is illustrated in Fig. 11. We can observe the following.

1) There is no obvious chattering phenomenon of the actual excitation voltage [see Fig. 11(a)], which indicates that the EERLSMC is capable of minimizing the chattering phenomenon prevalent in traditional SMCs.
2) The relationship between the normalized x_r, U and x [see Fig. 11(b)] demonstrates that the EERLSMC can generate an actual excitation voltage with inverse hysteresis features. Thus, it can remove hysteresis nonlinearity between U and x, linearizing the relationship between x_r and x.

Further, we employ the Planar DEAs, Conical DEA, and DEA-MES to track triangle trajectories with different slopes and amplitudes, shown in Fig. 12(a). We can see that they also can precisely track triangle trajectories with e_m and e_{rms} of less than 9.88% and 3.81%, respectively. In addition, the EERLSMC also has the capability to precisely track complex sinusoidal trajectories with changing amplitude and frequency [see Fig. 12(b)], demonstrating the effectiveness

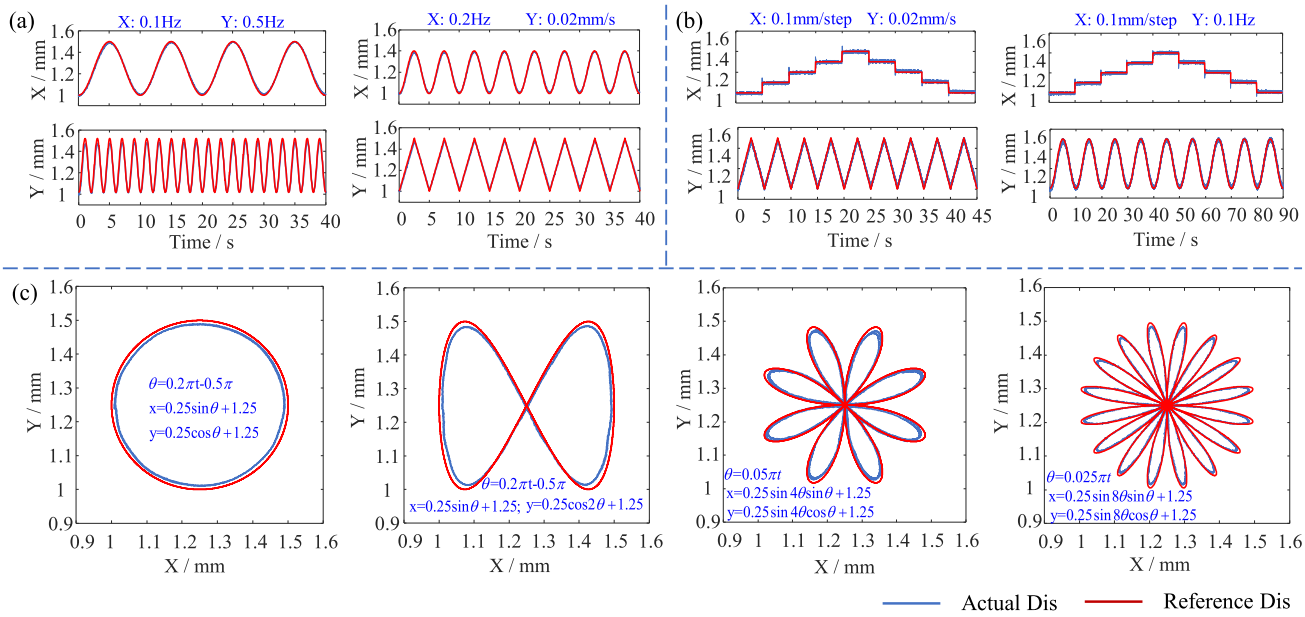

Fig. 13. Experimental results of tracking 2DOFs planar trajectories. (a) *X*-axis tracks sinusoidal trajectories while the *Y*-axis follows sinusoidal or triangle trajectories. (b) *X*-axis tracks step trajectories while the *Y*-axis follows sinusoidal or triangle trajectories. (c) 2DOF-DEA is used to draw complex pictures.

and generality of the EERLSMC for different DEAs and trajectories.

Remark: It should be noted that due to the digital process (sampling time 1 ms), the first derivative and second derivative of the triangle trajectories are discontinuous but bounded. Given that the discontinuous second derivative of the triangle trajectories lasts only 1 ms, it is essential to note that the influence on the actual voltage is further constrained by the rise time of the high-voltage amplifier. This time constraint ensures that the impact of the discontinuity is limited and does not significantly affect the resulting voltage applied to the DEAs. Therefore, when the slope of the triangle trajectories is relatively small (the maximum slope for planar DEAs, conical DEA and DEA-MES is limited to 0.5, 2.0, and 3.0 mm/s, respectively), the DEAs still can achieve high-precision tracking control. In this work, to verify the effectiveness of our development, we restrict the slopes of the triangle-like signals in different trajectory-tracking tests. Given that the primary emphasis of this work is on developing a generalized motion control framework for DEAs, a comprehensive analysis of the critical slope will be a subject of future investigation.

Lastly, by taking advantage of multiple DOFs, the 2DOF-DEA is capable of tracking complex planar trajectories (see Fig. 13). For example, when the *X*-axis generates sinusoidal trajectories with different frequencies, the *Y*-axis can follow both sinusoidal or triangle trajectories [see Fig. 13(a)], validating the decoupling ability of the designed EERLSMC. We also employ *X*-axis to track step trajectories while the *Y*-axis outputs a triangle or sinusoidal trajectories [see Fig. 13(b)]. In addition, by synthetic control of *X* and *Y* axes, the 2DOF-DEA can draw complex pictures, such as circle, butterfly, and flowers [see Fig. 13(c)]. These experimental results demonstrate that the 2DOF-DEA can achieve precise manipulation and movement, showing its potential applications in many fields, such as cell manipulation, Atomic Force Microscope, and Nano/Micro fabrications.

V. Conclusion

A successful experimental verification of the proposed generalized dynamic modeling and motion control framework has been demonstrated. The control-enabling nature of the proposed model has been demonstrated via a set of detailed experiments conducted on four different DEA configurations, two dielectric elastomer materials and two different DOFs. The implemented EERLSMC is shown to be capable of delivering precise trajectory tracking by effectively suppressing the undesirable, error-inducing effects of the inherent nonlinear dynamics of DEAs. Future work will focus on further exploiting the proposed control-enabling generalized framework to develop new high-performance control schemes, thereby expanding the scope of practical applications for DEAs.

In contrast to existing models for DEAs, our generalized dynamic model boasts the following distinctive features.

1) Diverging from identified linear systems, our dynamic model excels in capturing the intricacies of rate-dependent viscoelasticity and mechanical vibration.
2) Unlike prevalent lumped parameter models, our dynamic model exhibits the capability to autonomously adapt to DEAs with varying configurations, materials, and DOFs.
3) Beyond the confines of pure phenomenological models, our dynamic model excels in quantitatively characterizing the intertwined dynamics of viscoelasticity and mechanical vibration across a broad frequency spectrum.

We would like to mention that the electromechanical instability of DEAs usually leads to mutation of elastic force,

actuation force, viscoelastic force and output displacement in (4). As a result, (2) and (3) fail to describe elastic force and actuation force, respectively, resulting in loss of efficacy of our generalized dynamic model. Therefore, our generalized motion control framework needs to avoid the electromechanical instability of DEAs [9], same as general prerequisite of practical applications. Considering the generality and versatility of the proposed motion control framework, it has clear potential to be adopted for the dynamic modeling and precision control of other electromechanical force-based soft actuators. It is important to note that our generalized dynamic model, as presented in this work, does not explicitly incorporate the cross-coupling effect. This complex issue will be explored comprehensively in subsequent research endeavors.

REFERENCES

[1] G. Li et al., "Self-powered soft robot in the Mariana Trench," *Nature*, vol. 591, no. 7848, pp. 66–71, 2021.

[2] Y. Chen et al., "Controlled flight of a microrobot powered by soft artificial muscles," *Nature*, vol. 575, no. 7782, pp. 324–329, 2019.

[3] E. Hajiesmaili and D. Clarke, "Dielectric elastomer actuators," *J. Appl. Phys.*, vol. 129, no. 15, 2021, Art. no. 151102.

[4] D. Lee et al., "A wearable textile-embedded dielectric elastomer actuator haptic display," *Soft Robot.*, vol. 9, no. 6, pp. 1186–1197, 2022.

[5] L. Yin et al., "Soft, tough, and fast polyacrylate dielectric elastomer for non-magnetic motor," *Nature Commun.*, vol. 12, no. 1, pp. 1–10, 2021.

[6] X. Ji et al., "Untethered feel-through haptics using 18-μm thick dielectric elastomer actuators," *Adv. Funct. Mater.*, vol. 31, no. 39, 2021, Art. no. 2006639.

[7] Y. Chen, S. Xu, Z. Ren, and P. Chirarattananon, "Collision resilient insect-scale soft-actuated aerial robots with high agility," *IEEE Trans. Robot.*, vol. 37, no. 5, pp. 1752–1764, Oct. 2021.

[8] J. Zhang et al., "Robotic artificial muscles: Current progress and future perspectives," *IEEE Trans. Robot.*, vol. 35, no. 3, pp. 761–781, Jun. 2019.

[9] Z. Suo, "Theory of dielectric elastomers," *Acta Mechanica Solida Sinica*, vol. 23, no. 6, pp. 549–578, 2010.

[10] G. Gu, U. Gupta, J. Zhu, L.-M. Zhu, and X. Zhu, "Modeling of viscoelastic electromechanical behavior in a soft dielectric elastomer actuator," *IEEE Trans. Robot.*, vol. 33, no. 5, pp. 1263–1271, Oct. 2017.

[11] J. Zou, G. Gu, and L. Zhu, "Open-loop control of creep and vibration in dielectric elastomer actuators with phenomenological models," *IEEE/ASME Trans. Mechatron.*, vol. 22, no. 1, pp. 51–58, Feb. 2017.

[12] C. Cao et al., "Exploiting bistability for high-performance dielectric elastomer resonators," *IEEE/ASME Trans. Mechatron.*, vol. 27, no. 6, pp. 5994–6005, Dec. 2022.

[13] J. Zou and G. Gu, "High-precision tracking control of a soft dielectric elastomer actuator with inverse viscoelastic hysteresis compensation," *IEEE/ASME Trans. Mechatron.*, vol. 24, no. 1, pp. 36–44, Feb. 2019.

[14] T. He, X. Zhao, and Z. Suo, "Dielectric elastomer membranes undergoing inhomogeneous deformation," *J. Appl. Phys.*, vol. 106, no. 8, 2009, Art. no. 083522.

[15] T. Lu, C. Ma, and T. Wang, "Mechanics of dielectric elastomer structures: A review," *Extreme Mechanics Lett.*, vol. 38, 2020, Art. no. 100752.

[16] Z. Suo, X. Zhao, and W. Greene, "A nonlinear field theory of deformable dielectrics," *J. Mechanics Phys. Solids*, vol. 56, no. 2, pp. 467–486, 2008.

[17] F. Chen, K. Liu, Y. Wang, J. Zou, G. Gu, and X. Zhu, "Automatic design of soft dielectric elastomer actuators with optimal spatial electric fields," *IEEE Trans. Robot.*, vol. 35, no. 5, pp. 1150–1165, Oct. 2019.

[18] J. Zou and G. Gu, "Dynamic modeling of dielectric elastomer actuators with a minimum energy structure," *Smart Mater. Structures*, vol. 28, no. 8, 2019, Art. no. 085039.

[19] Y. Wang, X. Zhang, Z. Li, X. Chen, and C.-Y. Su, "Adaptive implicit inverse control for a class of Butterfly-like hysteretic nonlinear systems and its application to dielectric elastomer actuators," *IEEE Trans. Ind. Electron.*, vol. 70, no. 1, pp. 731–740, Jan. 2023.

[20] J. Zou and G. Gu, "Feedforward control of the rate-dependent viscoelastic hysteresis nonlinearity in dielectric elastomer actuators," *IEEE Robot. Autom. Lett.*, vol. 4, no. 3, pp. 2340–2347, Jul. 2019.

[21] G. Rizzello, D. Naso, A. York, and S. Seelecke, "Modeling, identification, and control of a dielectric electro-active polymer positioning system," *IEEE Trans. Control Syst. Technol.*, vol. 23, no. 2, pp. 632–643, Mar. 2015.

[22] T. Hoffstadt and J. Maas, "Adaptive sliding-mode position control for dielectric elastomer actuators," *IEEE/ASME Trans. Mechatron.*, vol. 22, no. 5, pp. 2241–2251, Oct. 2017.

[23] P. Huang, J. Wu, P. Zhang, Y. Wang, and C.-Y. Su, "Dynamic modeling and tracking control for dielectric elastomer actuator with a model predictive controller," *IEEE Trans. Ind. Electron.*, vol. 69, no. 2, pp. 1819–1828, Feb. 2022.

[24] Y. Wang et al., "Modeling and compound control of intelligently dielectric elastomer actuator," *Control Eng. Pract.*, vol. 126, 2022, Art. no. 105261.

[25] S. Hau, G. Rizzello, M. Hodgins, A. York, and S. Seelecke, "Design and control of a high-speed positioning system based on dielectric elastomer membrane actuators," *IEEE/ASME Trans. Mechatron.*, vol. 22, no. 3, pp. 1259–1267, Jun. 2017.

[26] J. MacLean et al., "Sliding-mode control of a dielectric elastomer actuator featuring non-invertible dynamics," in *Proc. 27th Int. Conf. Mechatron. Mach. Vis. Pract.*, 2021, pp. 1–6.

[27] Z. Ye and Z. Chen, "Modeling and control of a 2-DOF dielectric elastomer diaphragm actuator," *IEEE/ASME Trans. Mechatron.*, vol. 24, no. 1, pp. 218–227, Feb. 2019.

[28] J. Zou et al., "Proxy-based sliding-mode tracking control of dielectric elastomer actuators through eliminating rate-dependent viscoelasticity," *Smart Mater. Structures*, vol. 31, no. 10, 2022, Art. no. 104002.

[29] S. Mozayan, M. Saad, H. Vahedi, H. Fortin-Blanchette, and M. Soltani, "Sliding mode control of PMSG wind turbine based on enhanced exponential reaching law," *IEEE Trans. Ind. Electron.*, vol. 63, no. 10, pp. 6148–6159, Oct. 2016.

[30] G. Gu et al., "Soft wall-climbing robots," *Sci. Robot.*, vol. 3, no. 25, 2018, Art. no. eaat2874.

[31] J. Huang et al., "Sliding mode control of permanent magnet generator system based on improved exponential rate reaching law," *IET Electric Power Appl.*, vol. 14, no. 7, pp. 1154–1162, 2020.

[32] C. Fallaha, M. Saad, H. Kanaan, and K. Al-Haddad, "Sliding-mode robot control with exponential reaching law," *IEEE Trans. Ind. Electron.*, vol. 58, no. 2, pp. 600–610, Feb. 2011.

[33] V. Utkin and L. Hoon, "Chattering problem in sliding mode control systems," in *Proc. Int. Workshop Variable Struct. Syst.*, 2006, pp. 346–350.

[34] J. Rivera et al., "Super-twisting sliding mode in motion control systems," *Sliding Mode Control*, vol. 1, pp. 237–254, 2011.

[35] N. Ding, J. Zou, and G. Gu, "Design of dielectric-elastomer actuated XY stages with millimeter range and submicrometer resolution," in *Proc. Int. Conf. Manipulation, Autom. Robot. Small Scales*, 2020, pp. 1–6.

[36] J. Zou, P. Yan, N. Ding, and G. Gu, "Feedback-cascaded inverse feedforward for viscoelastic creep, hysteresis and cross-coupling compensation in dielectric-elastomer actuated XY stages," in *Proc. IEEE/ASME Int. Conf. Adv. Intell. Mechatron.*, 2020, pp. 2054–2061.

Jiang Zou (Member, IEEE) received the B.E. degree in mechanical engineering from the University of Science and Technology Beijing, Beijing, China, in 2014, and the Ph.D degree in mechanical engineering form Shanghai Jiao Tong University, Shanghai, China, in 2019.

Since 2019, he has worked with Shanghai Jiao Tong University. He is currently an Associate Professor with the School of Mechanical Engineering. His research interests have been focused on design, modeling, and control of dielectric elastomer actuated soft robots. He has authored or co-authored more than 25 publications, which have appeared in Science Robotics, Nature Communications, National Science Review, IEEE TRANSACTIONS ON ROBOTICS etc.

Shakiru Olajide Kassim received the National Diploma in 1995 and Higher National Diploma in 1998 in electrical and electronics engineering from the Federal Polytechnic Mubi, Mubi, Nigeria (both at Distinction level), the Postgraduate Diploma in 2004 and M.Eng degree in 2017 in electrical engineering (electronics) from the Prestigious Abubakar Tafawa Balewa University, Bauchi, Nigeria. He is currently working toward the Ph.D. degree in electrical engineering under the full sponsorship with the Petroleum Technology Development Fund (PTDF) and the Artificial Intelligence, Robotics, and Mechatronic Systems Group (ARMS), School of Engineering, University of Aberdeen, Aberdeen, U.K.

He has been a Teacher (Principal Lecturer) with the Department of Electrical/Electronics and Computer Engineering, Federal Polytechnic Damaturu, Damaturu, Nigeria, since 2009. His research interests include centers on control systems (development of control schemes for nonlinear soft robotic systems), digital systems, and signal processing.

Jieji Ren received the bachelor degree in optical information science and technology and master degree in optics from the Harbin Institute of Technology, Harbin, China, in 2013 and 2015, respectively, and the Ph.D. degree in mechanical engineering from Shanghai Jiao Tong University, Shanghai, China, in 2022.

He is currently working as the Postdoctoral Research with the Institute of Robotics, Shanghai Jiao Tong University. His research interests include vision-based tactile sensors, computer vision, and deep learning.

Vahid Vaziri received the B.Eng. degree in instrumentation and control from the Power and Water University of Technology, Tehran, Iran, in 2005, the M.Sc. degree in complex systems engineering from the University of Henri Poincaré, France, in 2010, and the Ph.D. degree in control and dynamics of nonlinear engineering systems from University of Aberdeen, U.K., in 2015.

He is currently a Senior Lecturer and a member of the Centre for Applied Dynamics Research (CADR), Artificial Intelligence, Robotics and Mechatronic Systems Group (ARMS) with the School of Engineering, University of Aberdeen, Aberdeen, U.K. He has more than 10 years of research experience and has authored or co-authored more than 50 peer-reviewed papers in the areas of dynamics and control of nonlinear engineering systems, such as drill-string, energy harvesting systems and rotor dynamics.

Sumeet S. Aphale (Senior Member, IEEE) was a Professor and the Director of the Artificial Intelligence, Robotics, and Mechatronic Systems Group with the School of Engineering, University of Aberdeen, Aberdeen, U.K. His research work has been authored in more than 110 peer-reviewed journal and conference publications, showcasing the depth and breadth of his work. With career spanning nearly two decades, he has focused his research on the system-level design, analysis, instrumentation, control, and experimental validation of robotic and mechatronic systems. which also includes subsea actuators, biomedical devices, renewable energy solutions, as well as sensing, and precision actuation technologies.

Prof. Aphale was the recipient of the best paper awards and nominations at several prestigious conferences for his research works. In recognition of his standing in the academic community, he has been an Associate Editor for IEEE CONTROL SYSTEMS LETTERS and *Frontiers of Mechanical Engineering* (Mechatronics).

Guoying Gu (Senior Member, IEEE) received the B.E. degree (with honors) in electronic science and technology, and the Ph.D. degree (with honors) in mechatronic engineering from Shanghai Jiao Tong University, Shanghai, China, in 2006 and 2012, respectively.

He is currently appointed as a Distinguished Professor with the School of Mechanical Engineering, Shanghai Jiao Tong University. He was a Humboldt Fellow with the University of Oldenburg, Oldenburg, Germany. He was a Visiting Scholar with the Massachusetts Institute of Technology, Cambridge, MA, USA, National University of Singapore, Singapore, and Concordia University, Montreal, Canada. He has authored or co-authored more than 100 publications, which have appeared in Science Robotics, Nature Biomedical Engineering, Nature Reviews Materials, Nature Materials, Nature Communications, Science Advances, IEEE/ASME Transaction, Advanced Materials, Soft Robotics, Science China serials etc., as book chapters and in conference proceedings. His research interests include soft robotics, bioinspired and wearable robots, smart materials sensing, actuation and motion control.

Dr. Gu was the recipient of the National Science Fund for Distinguished Young Scholars and the XPLORER PRIZE. He is currently an Associate Editor of *Soft Robotics* and was an Associate Editor for IEEE TRANSACTIONS ON ROBOTICS and IEEE ROBOTICS AND AUTOMATION LETTERS. He has also served for several journals as Editorial Board Member, Topic Editor, or Guest Editor, and several international conferences/symposiums as Chair, Co-Chair, Associate Editor, or Program Committee Member.